Computers and Geotechnics 126 (2020) 103733

Contents lists available at ScienceDirect

Computers and Geotechnics

journal homepage: www.elsevier.com/locate/compgeo

Research Paper

Pattern transitions of localized deformation in high-porosity sandstones: Insights from multiscale analysis

Huanran Wu[a,b], Jidong Zhao[b,*], Weijian Liang[b]

[a] School of Civil Engineering, Chongqing University, Chongqing 400045, China
[b] Department of Civil and Environmental Engineering, Hong Kong University of Science and Technology, Clearwater Bay, Kowloon, Hong Kong, China

ARTICLE INFO

In memory of Scott W. Sloan

Keywords:
Compaction band
Pattern transition
High-porosity rock
Critical state
FEM/DEM multiscale modeling

ABSTRACT

We employ a hierarchical multiscale modeling approach to investigate the transitions of localized deformation patterns in high-porosity sandstone subjected to sustained shear to understand their underlying physics. The multiscale approach is based on hierarchical coupling between finite element method (FEM) with discrete element method (DEM) to offer cross-scale predictions for granular rocks without assuming phenomenological constitutive relations. Our simulations show that when a high-porosity sandstone specimen is subjected to continuous deviatoric loading, compaction bands may occur and evolve, featuring a steady movement of the compaction front (i.e. the boundary between the compaction band and the rest uncompacted zone). The specimen reaches a homogeneous state of reduced porosity when the compaction fronts traverse the entire specimen. A re-hardening response is initiated in the specimen under further shear, which is followed by a shearing dominating stage with the emergence of shear bands. The material responses inside the ultimate shear bands approach a "steady state" of constant porosity and stress ratio. Cross-scale analyses reveal that debonding and pore collapse are dominant mechanisms for the compaction stage of the specimen, and debonding and particle rotation dictate the physics for the shear banding stage. The transitions from compaction to shear banding occurs due to the degradation of the cohesive contact network and significant reduction in porosity. There are limited number of interparticle bonds remaining at the "steady state" under sustained shear, with a preferential direction perpendicular to the loading direction, leading to a higher steady void ratio than the critical state void ratio of non-cohesive sand.

1. Introduction

Deformation bands, in forms of tabular zones with highly localized strain and small offsets, are ubiquitous in porous rocks in field outcrops (Aydin, 1978; Fossen, 2010). Their occurrence may significantly alter the porosity and permeability of a host rock and cause potential complications and even adverse effects to relevant engineering applications, ranging from reservoir operation and CO_2 geological sequestration to underground water resource management (Vajdova et al., 2004; Fossen and Bale, 2007; Haimson, 2007). Compaction Band (CB) is an end member of the kinematic spectrum of deformation patterns that has drawn special attentions from the community by its theoretical and practical importance since its field observation (Mollema and Antonellini, 1996; Holcomb et al., 2007). Experimental studies based on triaxial compression tests (Tembe et al., 2008; Baud et al., 2015) indicate that CB occurs frequently in high-porosity (with a porosity range of 13–28%) rocks and its formation is controlled by both loading conditions and material properties, e.g. the confining pressure, the degree of cementation, the grain size distribution and the heterogeneity of the specimen (Cheung et al., 2012; Fortin et al., 2006; Haimson, 2007). These findings have been further confirmed by both theoretical and computational studies, including those based on finite element method (FEM) and discrete element method (DEM) (Issen and Rudnicki, 2000; Buscarnera and Laverack, 2014; Das et al., 2014; Katsman et al., 2006; Liu et al., 2015).

It remains puzzling to the community, however, as to how and why only a limited number of CBs have been observed in field outcrops, e.g. in the Navajo Sandstone of Utah and in the Aztec Sandstone at the Valley of Fire State Park in Nevada (Mollema and Antonellini, 1996; Aydin and Ahmadov, 2009; Eichhubl et al., 2010; Schultz et al., 2010). Possible attributing reasons, according to past studies (Holcomb et al., 2007), include: (1) the difficulty to detect or recognize CB in a natural setting; (2) the required conditions of CB being rare in the earth. Theoretical studies suggested that axisymmetric compression is the most

* Corresponding author.
E-mail address: jzhao@ust.hk (J. Zhao).

https://doi.org/10.1016/j.compgeo.2020.103733
Received 17 March 2020; Received in revised form 27 June 2020; Accepted 1 July 2020

favorable stress condition for CB (Issen and Rudnicki, 2000) and a specific loading path might be required due to the dependency of material property on mean stress (Issen and Challa, 2008). Numerous laboratory tests have also been conducted in attempting to create suitable conditions for the occurrence of compaction bands. A particularly interesting phenomenon reported in triaxial compression experiments is the thickening of CB in width under sustained axial loading (Baud et al., 2004; Olsson, 2001), in contrast to the concentration of deformation inside finite width for shear band (SB) (Jiang et al., 2011; Gao and Zhao, 2013). The fact that SB may occur at a denser state than the post-CB state in a sandstone suggests a third possibility. CB may occur in the same sandstone as a transition of pattern when compaction fronts spread throughout a specimen, which is followed by re-hardening under continuous shear to meet the SB conditions. This transition of patterns is compatible with experimental observations and the theoretical prediction (Wong et al., 1992; Olsson, 1999), and offers a possible explanation for the infrequency in field observation of CB.

Unfortunately, in the majority of existing experimental tests, the specimens have only been loaded up to the CB stage or early re-hardening stage (Baud et al., 2012; Olsson, 1999), which precludes the observation of deformation pattern transitioning to shear bands. One exception is a recent experimental study on Tuffeau de Maastricht which indeed reported the transition from CB to SB in a specimen subjected to triaxial compression of axial strain up to 50% (Papazoglou, 2018). Shahin et al. (2019) has offered a numerical prediction of the evolution of compaction zones and the global responses up to the homogeneous re-hardening stage based on FEM simulations with an elastoplastic constitutive law. It remains tremendously challenging, both numerically and experimentally, to capture and characterize the transition of localization patterns in porous rocks to understand the underlying mechanisms.

In this study, we employ a recently developed multiscale approach based on coupled FEM with DEM (Guo and Zhao, 2014) to tackle this challenge. In this scheme, a macroscale boundary value problem is solved by FEM. A representative volume element (RVE) consisting of discrete particles is attached at each Gauss point of the FEM mesh. Each RVE packing receives displacement gradients at its corresponding Gauss point from FEM as boundary conditions and allows DEM to compute for a solution and produce homogenized stresses and tangent operator for the global FEM solution. The adoption of DEM computations for material responses helps bypass the necessity for phenomenological constitutive model while respecting the discrete nature of granular materials, and facilitates direct linking between the macroscale phenomena and their underlying microscale mechanisms. This approach has been employed to investigate various aspects of complex material and structural responses of granular materials, including anisotropy, non-coaxiality, deformation localization (Zhao and Guo, 2015; Guo and Zhao, 2016a; Guo et al., 2016). Its further extension for cohesive granular materials has enabled the authors to successfully capture CB in high-porosity granular rocks under various loading conditions (Wu et al., 2018a,b, 2019). Debonding and pore collapse have been identified as two major micromechanisms in the absence of grain crushing, and they indeed convert the specimen to a partially cohesive state of lower porosity. This study will continue this line of work and focus on further evolution of CB under sustained axial loading into re-hardening and possible transition to SB.

2. Methodology

A hierarchical multiscale approach is employed for the following study (Guo and Zhao, 2014). In this approach, a FEM solver (an open-source code esys-escript in current scheme (Schaa et al., 2016)) is adopted to discretize the macroscale domain of a boundary value problem and pass the deformation gradient at each Gauss point to the corresponding RVE as the mesoscale boundaries. A DEM solver (Yade in current scheme (Smilauer et al., 2015)) is employed to solve the mesoscale BVP for the RVE and feed back the FEM solver with homogenized stress and tangent operator from the deformed RVE. This scheme avoids assumption of phenomenological constitutive relationship commonly needed by conventional continuum modeling, while respecting the discrete nature of cohesive granular rocks. It can naturally capture the conversion from cohesive material to non-cohesive material due to debonding. To avoid excessive repeat, the interested readers are referred to Guo and Zhao (2014) and Wu et al. (2018a) for detailed formulations, solution algorithms and the adaptation for granular rocks. Relevant researches on this approach can also be found in Guo and Zhao (2016b,c), Desrues et al. (2017), Liu et al. (2016), Shahin et al. (2016), Argilaga et al. (2018), Wang and Sun (2016) and Desrues et al. (2019), regarding the mesh dependency, RVE variability, computational performance, and the extensions to solve three dimensional or hydro-mechanical coupling problems.

2.1. RVE preparation

Essential to the coupled FEM/DEM approach is to prepare a RVE that represents the targeting material and provides the mechanical responses. Particle crushing has been regarded as an important micromechanism observed in laboratory tests of compaction band in sandstones. However, field observations suggest that compaction band may form with much fewer and less severe grain crushing. Image analysis of compaction bands in Tuffeau de Maastricht shows mainly intragranular fractures without intense grain crushing (Papazoglou, 2018). Indeed, the authors have reproduced compaction band in biaxial compression and borehole instability analyses with high-porosity RVEs consisting of non-crushable particles and demonstrated that debonding and pore collapse may serve as possible major micromechanisms (Wu et al., 2017, 2018a,b). A similar high-porosity RVE as in these previous studies, consisting of 749 circular non-crushable particles, is employed in this study to investigate the evolution of compaction band with sustained axial strain.

The high-porosity structure (porosity: 0.326), as presented in Fig. 1, is generated by removing pre-inserted large particles and rattlers with less than one contact. Interparticle cohesion is added before the removals to maintain a stable structure. The interparticle cohesion is governed by a maximum tensile force ($F_n^{\max} = c\min(r_1, r_2)^2$, where c is the cohesion strength, and r_1 and r_2 are the radii of the two particles in contact) and a maximum shear force ($F_s^{\max} = c\min(r_1, r_2)^2 + F_n\tan\phi$, where ϕ is interparticle friction angle). If either of the two is exceeded, the cohesion will be eliminated and the contact becomes pure frictional

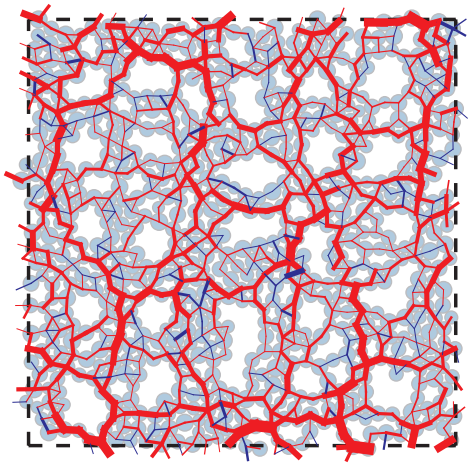

Fig. 1. High-porosity RVE consisting of bonded, non-crushable circular particles, where the dashed rectangle represents the periodic boundaries and the short line segments indicate interparticle normal force (red for compressive contacts and blue for tensile ones). (For interpretation of the references to color in this figure legend, the reader is referred to the web version of this article.)

Table 1
Calibrated DEM modeling parameters for particles in the RVE (Wu et al., 2019).

Parameter	Value
Cohesion strength c (GPa)	6.8
Particle radii r (mm)	0.2–0.3
Interparticle friction angle ϕ (°)	35
Stiffness parameter E_c (GPa)	950
Shear/normal stiffness ratio ν_c	1.0

and governed by a linear force–displacement law and Coulomb-type friction (i.e. $F_s \leqslant F_n \tan\phi$). The normal contact stiffness is derived as $k_n = E_c \times \frac{2r_1 r_2}{r_1 + r_2}$ and the shear stiffness as $k_s = \nu_c k_n$, where E_c and ν_c are two user-defined parameters. The calibrated parameters of the DEM particles are listed in Table 1. The particle radii (r) follow a linear distribution between 0.2 and 0.3 mm, mimicking the well-sorted Berea sandstone with a mean grain radius of 0.25 mm (Haimson, 2003). The interparticle friction angle (ϕ) and the shear/normal stiffness ratio (ν_c) are common values in DEM models for sandstones and sands. The stiffness parameter (E_c) and cohesion strength (c) are calibrated to reach a uniaxial compressive strength (UCS) of 24.9 MPa and Young's modulus (E) of 11.0 GPa, which are close to the corresponding values of Berea sandstone (porosity: 0.25 ± 0.01, UCS: 24 ± 2 MPa) and Mansfield sandstone (porosity: 0.26 ± 0.01, UCS: 22.4 ± 0.5 MPa, E: 9.6 ± 0.1 GPa) (Haimson, 2003; Haimson and Lee, 2004). Interested readers are referred to Wu et al. (2018b,a, 2019, 2020a) for more details of this RVE, and the influence of RVE properties and loading conditions on the localization patterns.

2.2. Model set-up for biaxial compression

We consider a high-porosity sandstone subjected to biaxial compression which is widely considered a favourable condition to form deformation bands. The FEM mesh and the applied boundary conditions are illustrated in Fig. 2. The entire domain is discretized into 12×20 eight-node quadrilateral elements. A reduced integration scheme with four Gauss points is adopted to reduce the computational cost while maintaining a good accuracy as compared to the full integration scheme (Zhao and Guo, 2015). The current FEM/DEM has been based on a non-regularized FEM formulation which may suffer mesh-dependency. To totally resolve this issue demands advanced regularization techniques such as those based on Cosserat continuum or second-order gradient (Desrues et al., 2019), which is beyond the scope of the present study. Nevertheless, mesh-dependency analyses have proved that the adoption of eight-noded quadrilateral elements is helpful to mitigate the mesh-dependency and produce relatively reliable post-peak behaviors with reasonably fine mesh, including the stress–strain relation, deformation band angle, transition of localization patterns and microscale responses, although the deformation band width still depends on mesh size (Guo and Zhao, 2016a; Wu et al., 2019, 2020a).

In laboratory experiments, compaction bands have been observed, either initiating from the middle of the specimen due to inherent heterogeneity (Fortin et al., 2006) or from the ends due to end friction (Olsson and Holcomb, 2000; Townend et al., 2008). Two extreme cases are investigated here — one with a smooth and the other with a rough loading platen. In the smooth case, the top and bottom boundaries are smooth with no lateral constraints. The bottom center is fixed to ensure the attainment of a converged solution. Two weak points (with a reduced cohesion strength c of 80% of the normal value) are inserted in the specimen to trigger the localization (see Fig. 2a). In the rough boundary case, the top and bottom boundaries are considered totally rough with no lateral displacement (see Fig. 2b). The lateral confining pressure is kept constant during the entire loading process in both cases. The top loading platen is pushed down with a nominal loading rate of 0.01% per quasi-static loading step.

3. Transition of deformation patterns from compaction band to shear band

Compaction bands have been observed from our simulation in specimens prepared with the RVE in Fig. 1 under biaxial compression of $\sigma_0 = 40$ MPa, in which ϵ_1 is up to 2.0% (Wu et al., 2019). Under dry or drained conditions, the compaction band will evolve to become thicker in width as the axial strain increases (Wu et al., 2019; Olsson, 1999; Baud et al., 2004). Since transitional behaviour is a major interest of the study, the focus of the following discussion is placed on the response of

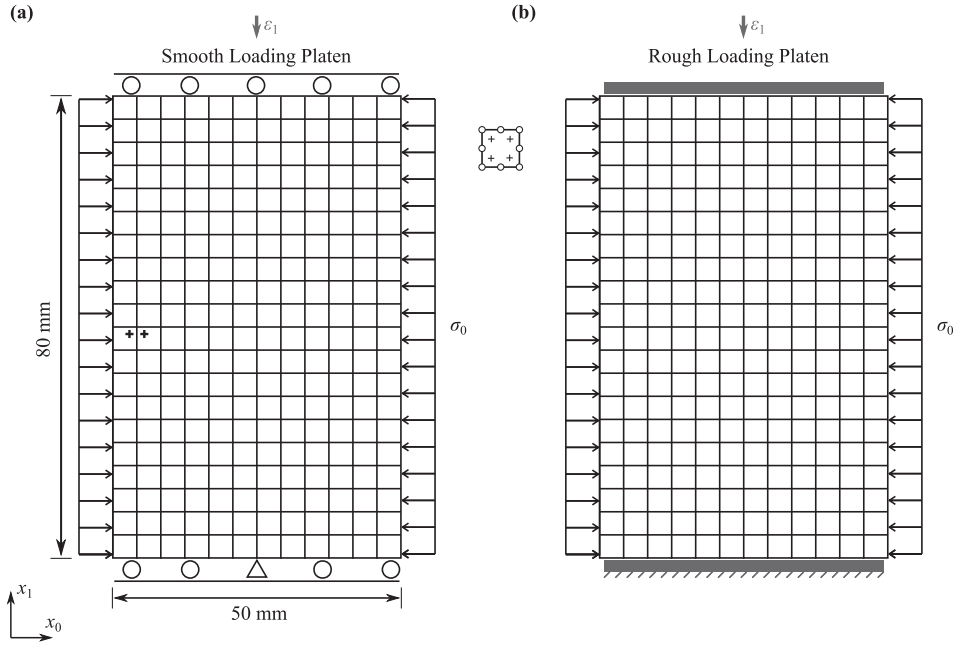

Fig. 2. FEM mesh with eight-node quadrilateral elements and boundary conditions for (a) the smooth case and (b) the rough case. The two crosses in (a) mark the location of the weak points.

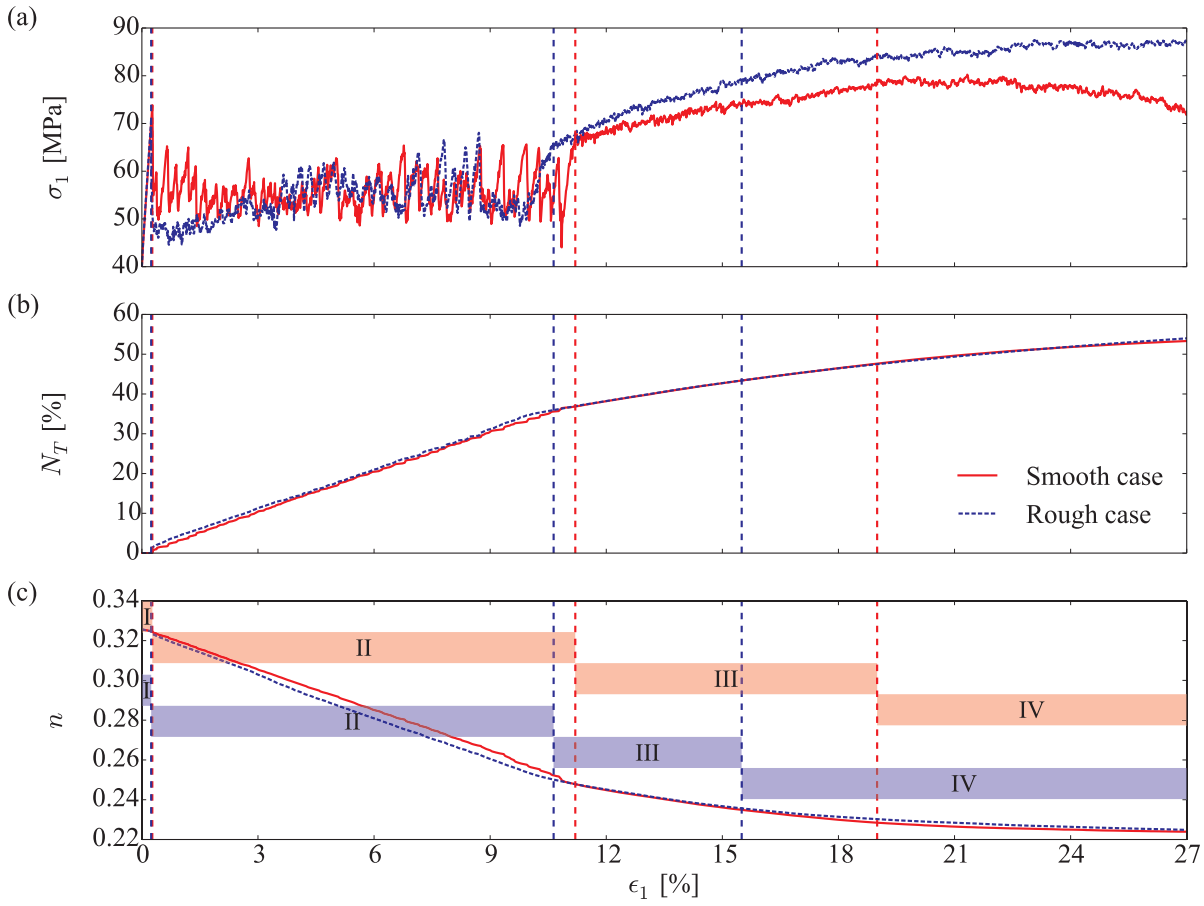

Fig. 3. The evolutions of axial stress (σ_1), global debonding number (N_T, normalized by initial bond number within the specimen) and average porosity (n) with increasing axial strain (ϵ_1) in both cases. The vertical dashed lines bound the four stages in each case.

the specimen under sustained axial loading going beyond the axial strain level at which the CB has traversed the entire specimen.

3.1. Evolution of global quantities

The global responses of the specimen in both cases are presented in Fig. 3 in terms of axial stress (σ_1), global debonding number (N_T, normalized by initial bond number within the specimen) and average porosity (n) with axial strain (ϵ_1) increased up to 27%. Despite some minor differences, the two cases present overall similar responses which can be broadly characterised by four stages:

1. Stage I: elastic stage. Both smooth and rough platen cases present almost identical pre-failure behavior with less than 2% difference in stiffness, almost no debonding events and a small decrease in n. The stress peak appears marginally earlier in the rough case than in the smooth case.
2. Stage II: CB stage. A brittle stress drop appears in the smooth case after the stress peak, followed by a plateau with apparent fluctuations. The rough case displays a more significant stress drop, followed by a gradual buildup of σ_1 to reach a stress plateau similar to the one in the smooth case. For both cases, N_T increases linearly while n decreases linearly during this stage, indicating a steady propagation of CBs. The CB stage ends with an apparent increase in σ_1 to a relatively large value, which occurs earlier in the rough case than in the smooth case.
3. Stage III: re-hardening stage. The re-hardening stage features a gentle linear build-up of σ_1. The rate of the build-up is higher and the re-hardening stage ends much earlier in the rough case than in the smooth case. N_T continues to increase and n to decrease, both at a lower rate than in the CB stage.
4. Stage IV: SB stage. The build-up rate of σ_1 begins to decrease at the beginning of SB stage. The two cases display a marked difference during SB stage in terms of σ_1. A decrease in σ_1 is observed in the smooth case, distinct from the gentle build-up to a quasi-steady value in the rough case. Nevertheless, N_T and n display similar features for both cases — N_T increasing and n decreasing, both at a decreasing rate, and evolving to quasi-steady values.

3.2. Evolution of localization pattern

The distinctive variations in global responses at different stages reflect the evolution of localization patterns with increasing axial strain. To examine the key features, we plot in Figs. 4 and 5 the contours of local quantities, including debonding number (N, normalized by initial bond number within an RVE), porosity (n), deviatoric strain (ϵ_q) and average particle rotation (θ) at selected axial strain levels for the smooth case and the rough case, respectively.

3.2.1. Smooth boundary case

The evolution of localization pattern for the smooth case is presented in Fig. 4. A single CB initiates from the pre-inserted weak points and penetrates through the specimen after the stress peak. A mature localization pattern at $\epsilon_1 = 3.0\%$ is presented in Fig. 4a–d. A consistent CB is observed from the contours of N, n and ϵ_q. The particle rotation θ in the CB is negligibly small thus Fig. 4d does not exhibit a clear pattern. The specimen is clearly partitioned into a compacted zone (CB) sandwiched by two uncompacted zones. The boundaries between the compacted and the uncompacted zones are commonly named as "compaction front" (Olsson, 2001). They propagate outwards with the

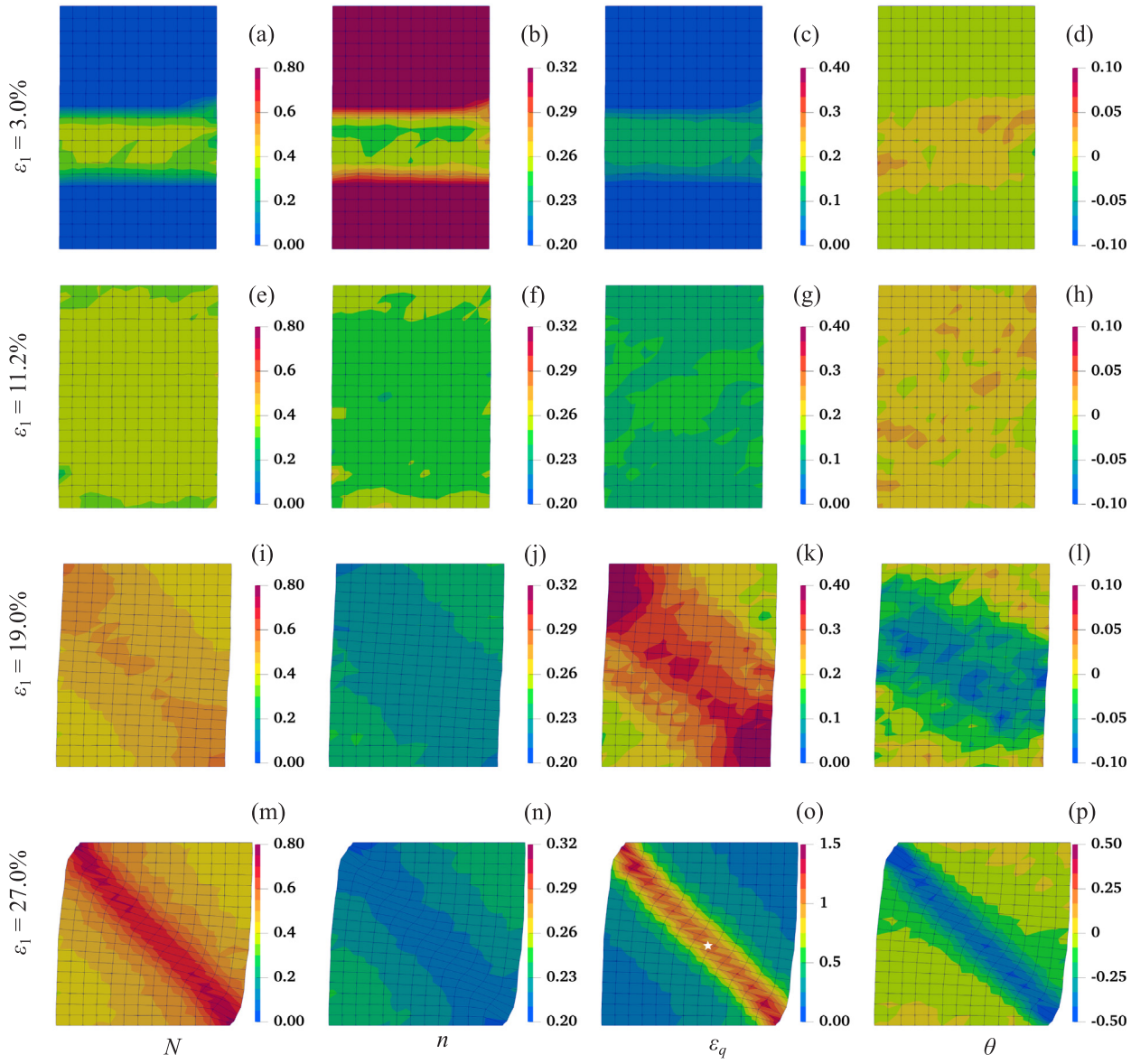

Fig. 4. Contours of debonding number (N, normalized by initial bond number in an RVE), porosity (n), deviatoric strain (ϵ_q) and average particle rotation (θ) at different axial strain levels for the smooth case.

increase of ϵ_1, leading to widening of CB until the compaction fronts reach both ends of the specimen, which marks the end of the pure CB stage. The whole specimen is subsequently compacted to an almost homogeneous state as presented in Fig. 4e–h.

A re-hardening stage follows the CB stage with gentle build-up of σ_1. A pre-mature SB is perceptible at the end of the re-hardening stage as presented in Fig. 4i–l, despite relatively low shear intensity. Localization of SB dominates the subsequent responses of the specimen. A noticeable SB with intensely localized shear strain and particle rotation at the final state is presented in Fig. 4m–p, indicated especially by the maximum ϵ_q of 150% and the minimum θ of -0.5 in Fig. 4o–p. The SB causes intense in-band debonding, evidenced by almost doubled increase in N from around 0.38 at the end of the CB stage to around 0.72 within the SB at the final state. However, the volumetric contraction caused by the SB is relatively mild. n merely decreases from 0.326 at the initial state to around 0.25 at the end of the CB stage, and further drops to around 0.21 within the SB at the final state.

3.2.2. *Rough boundary case*

As presented in Fig. 3, the global responses of the rough boundary case are qualitatively similar with the smooth case with some differences. The localization patterns at selected axial strain levels for the rough case are presented in Fig. 5 in contrast with the smooth case in Fig. 4. Two CBs initiate from the top and bottom boundaries respectively in the rough case, evolve to reach a mature pattern at $\epsilon_1 = 3.0\%$ as is presented in Fig. 5a–d. The compaction fronts at the top and the bottom move towards each other with increasing axial strain. They meet each other at the end of the CB stage before the whole specimen is further compacted to a homogeneous state as presented in Fig. 5e–h. In contrast to the single SB in the smooth case, a pair of pre-mature SBs are perceptible at the end of the re-hardening stage as presented in Fig. 5i–l. Further localization of this pair of SBs dominates the responses of the specimen afterwards in the final SB stage. The mature SBs at the final state are displayed in Fig. 5m–p, displaying a rather symmetric crossed shape with intense shear strain and particle rotation.

Evidently, both the smooth and the rough boundary cases present qualitatively similar global responses with elastic stage, CB stage, re-

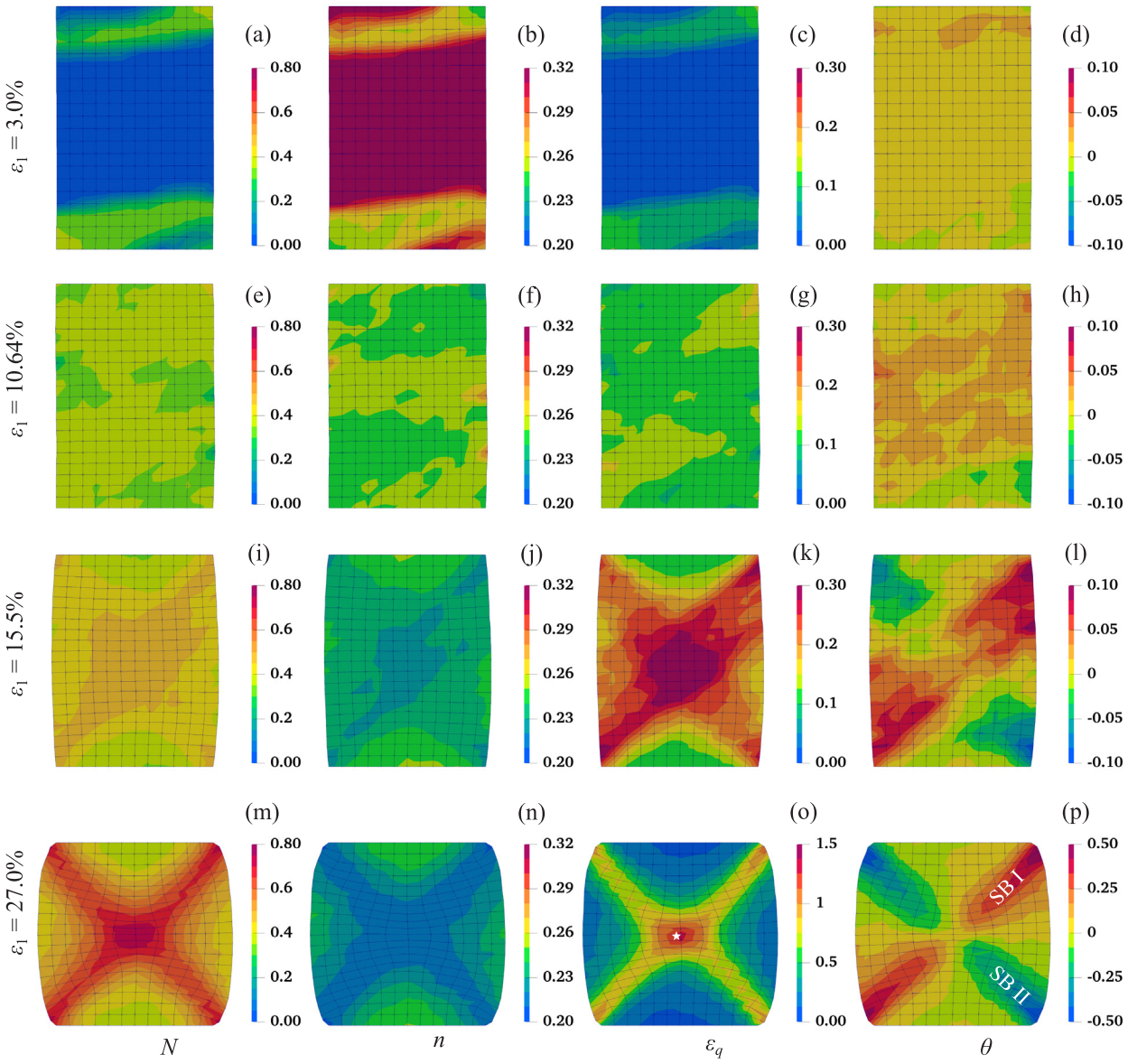

Fig. 5. Contours of debonding number (N, normalized by initial bond number in an RVE), porosity (n), deviatoric strain (ϵ_q) and average particle rotation (θ) at different axial strain levels for the rough case.

hardening stage and SB stage. As compared to the smooth case, the stress drop after the peak for the rough case is higher, which is attributed to the initial inclined CBs (inclination angle less than 10°), and the CB stage ends earlier due to the lateral constraint from the rough boundaries (a higher confinement near the boundaries). In both cases, the specimen is compacted to a roughly homogeneous state at the end of the CB stage with normalized global debonding number (N_T) around 35% and average porosity (n) around 0.25. The subsequent responses of the specimen, characterized by a re-hardening stage followed by a SB stage, is similar to cemented sand (Jiang et al., 2011; Wang and Leung, 2008). A reduction in σ_1, accompanied by a single SB, is found in the SB stage of the smooth case. In contrast, σ_1 builds up gently to a quasi-steady value in the rough case with the formation of a pair of symmetric cross-shaped SBs.

4. Transition mechanisms: insights from cross-scale analyses

The global responses of the specimen could be categorised into two major regimes: (a) the initiation and evolution of CBs (Stages I and II); (b) the transition to SBs and further development (Stages III and IV). Regime (a) exhibits typical mechanical responses of high-porosity rock under relatively high confinement, featuring the propagation of compaction fronts. It ends when the entire specimen undergoes substantial compaction and enters a relatively homogeneous state of lower porosity of around 0.25. Regime (b) represents the subsequent responses of a relatively denser geomaterial with certain remnant bonds, featuring the formation and progressive evolution of SBs. The associated physical mechanisms with the two regimes will be discussed in the following based on thorough cross-scale analyses of the multiscale simulation results.

4.1. Propagation of compaction fronts

A common feature can be identified from the evolution of compaction bands in both cases presented above: the compacted region is delineated from the uncompacted region by a moving compaction front which is roughly perpendicular to the loading direction. Indeed, similar phenomena have been reported in dynamic compaction of snow and cereal packs (Guillard et al., 2015; Barraclough et al., 2016). To visualize the advancing of compaction fronts, we adapt the spacial-

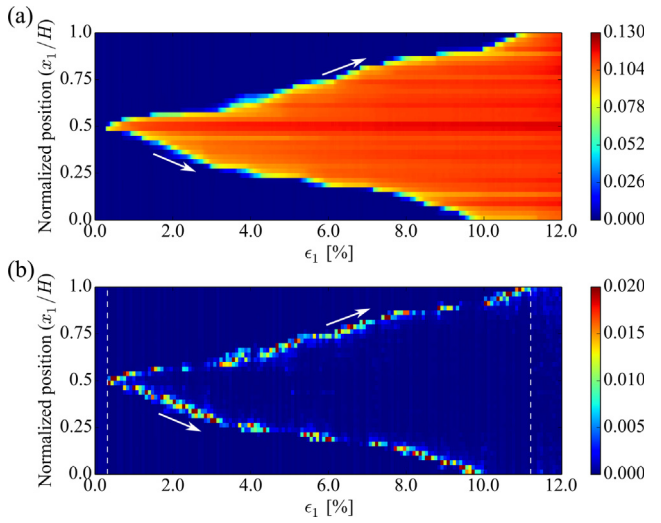

Fig. 6. The propagation of compaction fronts for the smooth boundary case in terms of (a) accumulated volumetric strain (ϵ_v) and (b) incremental volumetric strain ($\Delta\ \epsilon_v$).

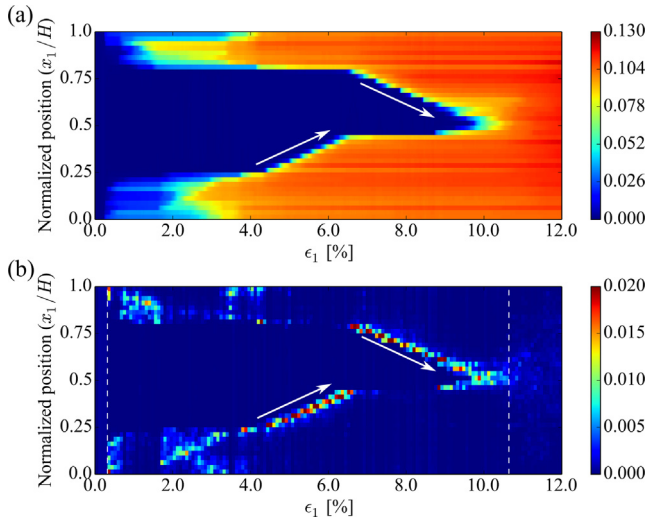

Fig. 7. The propagation of compaction fronts for the rough case in terms of (a) accumulated volumetric strain (ϵ_v) and (b) incremental volumetric strain ($\Delta\ \epsilon_v$).

temporal plots from Barraclough et al. (2016), where the accumulated and incremental volumetric strain (ϵ_v and $\Delta\ \epsilon_v$) are averaged over x_0 coordinate and plotted in color-scale as a function of x_1 and ϵ_1 (Fig. 6 for the smooth case and Fig. 7 for the rough case). Following Lagrangian coordinates, x_1 is normalized by the initial height of the specimen (H) to indicate the relative position along the loading direction in the initial undeformed configuration. ϵ_1 denotes the pseudo time given the constant loading rate.

The plots for ϵ_v depict a clear contrast between strong localization (red) of ϵ_v perpendicular to the loading direction and weak or non-compaction regime (blue). The blur boundaries at the early stage in Fig. 7a (from $\epsilon_1 = 0.24\%$ to $\epsilon_1 = 4\%$) reflect the initial inclined localization bands. In both cases, the expansion of red zone along the ϵ_1 axis indicates the enlargement of the compacted region under the axial loading. The inclined boundaries between the red and blue zones reflect the movement of the compaction fronts where the slope in the figure defines the velocity of the movement. The plots for $\Delta\ \epsilon_v$ show the positions of compaction fronts and their movement. It is interesting to note that the magnitude of $\Delta\ \epsilon_v$ in regions rather than the compaction fronts are vanishingly small, indicating that localized compaction occurs only at the compaction fronts. Despite the presence of two compaction fronts in both cases, several segments of varying constant slope are notable in Figs. 6 and 7, indicating that the movement of one compaction front may be at a constant velocity while the other is on hold (see the white arrows) for certain strains. Indeed, the two compaction fronts in the rough boundary case appear to propagate in an alternating manner according to our simulations.

We herein simplify the two compaction fronts to a single composite one moving downwards from the top to the bottom of the specimen. Its average velocity (pseudo velocity regarding ϵ_1 as pseudo time for the quasistatic loading condition given the constant loading rate), as compared to the velocity of the platen, can be evaluated based on the duration of the CB stage following:

$$\frac{v_\Gamma}{v_P} = \frac{1-\epsilon_I}{\epsilon_E - \epsilon_I} \tag{1}$$

where v_Γ is the velocity of the compaction front, v_P is the velocity of the loading platen, ϵ_I and ϵ_E are the levels of ϵ_1 at the initiation and the end of the CB stage, respectively. Indeed, in discussing the quasistatic propagation of compaction fronts in porous rock, Olsson (2001) has derived the following velocity ratio for a compaction front moving along the loading direction based on mass balance which is similar to Eq. (1):

$$\frac{v_\Gamma}{v_P} = \frac{1-n}{n_0 - n} \tag{2}$$

where n is the porosity of the compacted region and n_0 is the original porosity. In Olsson (2001), a prediction of $v_\Gamma/v_P = 11.3$ is obtained following this simplified model, in contrast to the measurement of $v_\Gamma/v_P = 8.3$ based on acoustic emission data.

Assuming a constant porosity inside the CB (see Fig. 4a and e), ϵ_E could be predicted based on ϵ_I and the porosity by combining Eqs. (1) and (2) following:

$$\epsilon_E = \epsilon_I + \frac{n_0 - n}{1-n} \times (1-\epsilon_I) \tag{3}$$

The velocities of a single composite compaction front derived following Eqs. (1) and (2) and the predicated ϵ_E following Eq. (3) for the two cases are summarized in Table 2. Evidently, the predicted velocities (v_Γ^2) following Eq. (2) agree well with the evaluations based on Eq. (1) (v_Γ^1). The predicted axial strain levels at the end of the CB stage (ϵ_E^p) based on the porosity reduction agree also well with the observations in our multiscale simulations.

4.2. Transition from compaction to shear band

Unlike the oscillatory propagation of compaction fronts observed in experiments on puffed rice packs (Valdes et al., 2012; Guillard et al., 2015) and dry foamed snow (Barraclough et al., 2016), the specimen in our numerical study transits to a SB stage through a continuous re-hardening stage after the two initial compaction fronts meet each other or reach the boundaries, i.e. after the entire specimen is compacted to a relatively homogeneous state of lower porosity.

4.2.1. Evolutions of mesoscale quantities

The multiscale approach enables us to directly connect our macroscopic observations with their microstructural mechanisms at the mesoscale. To this end, we present in Fig. 8 the homogenised mesoscale responses of selected RVEs from inside and outside SB to examine the key material origins during the transition from the CB stage throughout the re-hardening stage and further to the SB stage. The two dashed

Table 2
Velocity of the composite compaction front and the prediction of ϵ_E.

Case	ϵ_I (%)	ϵ_E (%)	v_Γ^1/v_P	n_0	n	v_Γ^2/v_P	v_Γ^2/v_Γ^1	ϵ_E^p (%)	ϵ_E^p/ϵ_E
Smooth	0.27	11.2	9.1	0.326	0.248	9.7	1.06	10.59	0.95
Rough	0.24	10.64	9.6	0.326	0.250	9.9	1.03	10.29	0.97

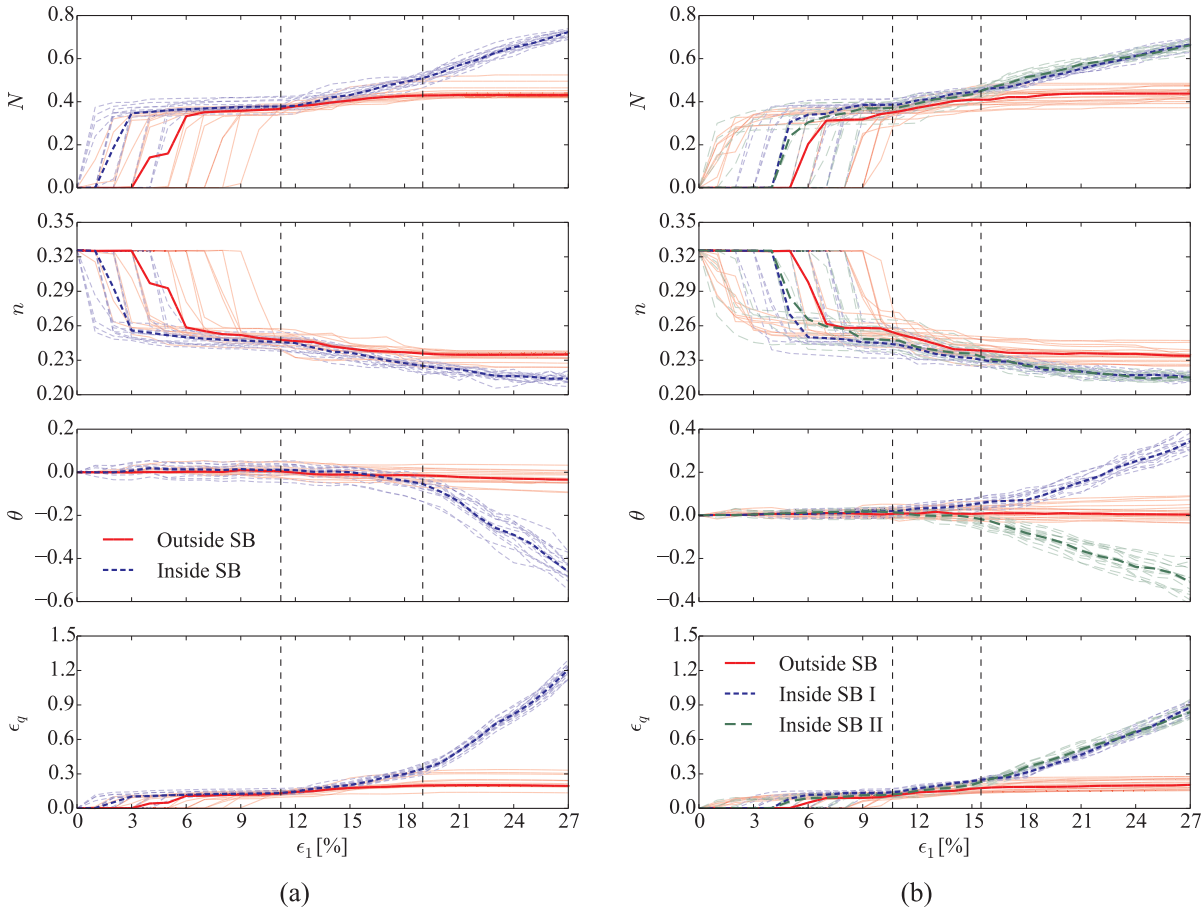

Fig. 8. The evolutions of local debonding number (N, normalized by initial bond number), porosity (n), average particle rotation (θ) and deviatoric strain (ϵ_q) with axial strain (ϵ_1) for (a) the smooth case and (b) the rough case at selected RVEs. The two dashed vertical lines mark the end of the CB stage and the beginning of the SB stage, respectively.

vertical lines in the subfigures mark the end of the CB stage and the beginning of the SB stage, respectively. The translucent lines are the responses of the selected individual RVEs, with a centre thicker, non-translucent line indicating their median in each case.

The RVE responses exhibit typical features of compaction bands at the CB stage in both cases, including great volume contraction (n) accompanied by intense debonding (N), small shear (ϵ_q) and no apparent rotation (θ). The responses of the RVEs begin to bifurcate gradually in the re-hardening stage and become more distinct in the SB stage. The behavior of RVEs in the two cases is qualitatively similar, though RVEs inside the SB present larger shear and rotation in the smooth case than in the rough case in the SB stage. In both cases, a volume contraction, accompanied by an increase in both N and ϵ_q, is observed at the re-hardening stage for RVEs outside the SB. Afterwards, all the quantities remain constant during the SB stage. On the other hand, N shows a linear increase and n displays a linear decrease for RVEs inside the SB during the re-hardening stage, while ϵ_q builds up slowly in the meanwhile. The build-up accelerates as the specimen enters the SB stage and reaches a constant rate thereafter. Interestingly, θ of the RVEs inside the SB remains close to zero until the late re-hardening stage, and presents a linear trend, either increasing or decreasing, at the SB stage. The development of θ lags behind that of ϵ_q, indicating that the deflection of average particle rotation is a consequence of shear band instead of the opposite. N increases linearly at a marginally higher rate in the SB stage than in the re-hardening stage. On the contrary, n drops at a decreasing rate and reaches constant at the final state.

4.2.2. Characteristics of steady states versus critical state in soil mechanics

The constant n attained at the final state in our simulations of sandstone reminds us of the "critical state" in soil mechanics (Schofield and Wroth, 1968; Zhao and Guo, 2013) when a cohensionless sand reaches a state of constant volume and constant stresses under sustained shear. To explore the difference, we first plot in Fig. 9 the evolutions of N, n, θ and stress ratio (q/p, where q and p are the deviatoric stress and the mean stress, respectively) with ϵ_q. The open circles and diamonds mark the end of the CB stage and the beginning of the SB stage, respectively. Again, the translucent lines represent the responses of selected individual RVEs and the nontransparent ones are their median values (based on the same ϵ_1). Notably, all the RVEs respond similarly with respect to ϵ_q during the CB stage. N increases linearly to around 0.4 and n decreases linearly to around 0.25 without apparent particle rotation. q remains largely constant during the linear contraction of the RVE and increases slightly at the end of the contraction. The responses of RVEs located inside shear band and outside shear band diverge from one another from the re-hardening stage. Specifically, the RVEs located outside the SB continue to contract at a decreasing rate, accompanied by gentle debonding, and cease to experience volume change at ϵ_q around 0.2. Their stress levels (q/p) are increasing over the re-hardening stage. During the SB stage, these RVEs experience unloading (decrease in q/p) in the smooth case, but unloading is not apparent for the rough case. On the other hand, RVEs located inside the SB undergo larger shear strain (to around 0.3) in the re-hardening stage and the shear strain reaches more than 0.8 at the final state in both cases. θ remains around 0 at the early re-hardening stage and then shows a linear trend (either increasing or decreasing) thereafter towards the end of loading. In the re-hardening stage, a build-up of q/p is notable accompanied by a decrease in n and increase in N, both at a decreasing rate. Notably, both q/p and n reach steady states at the SB

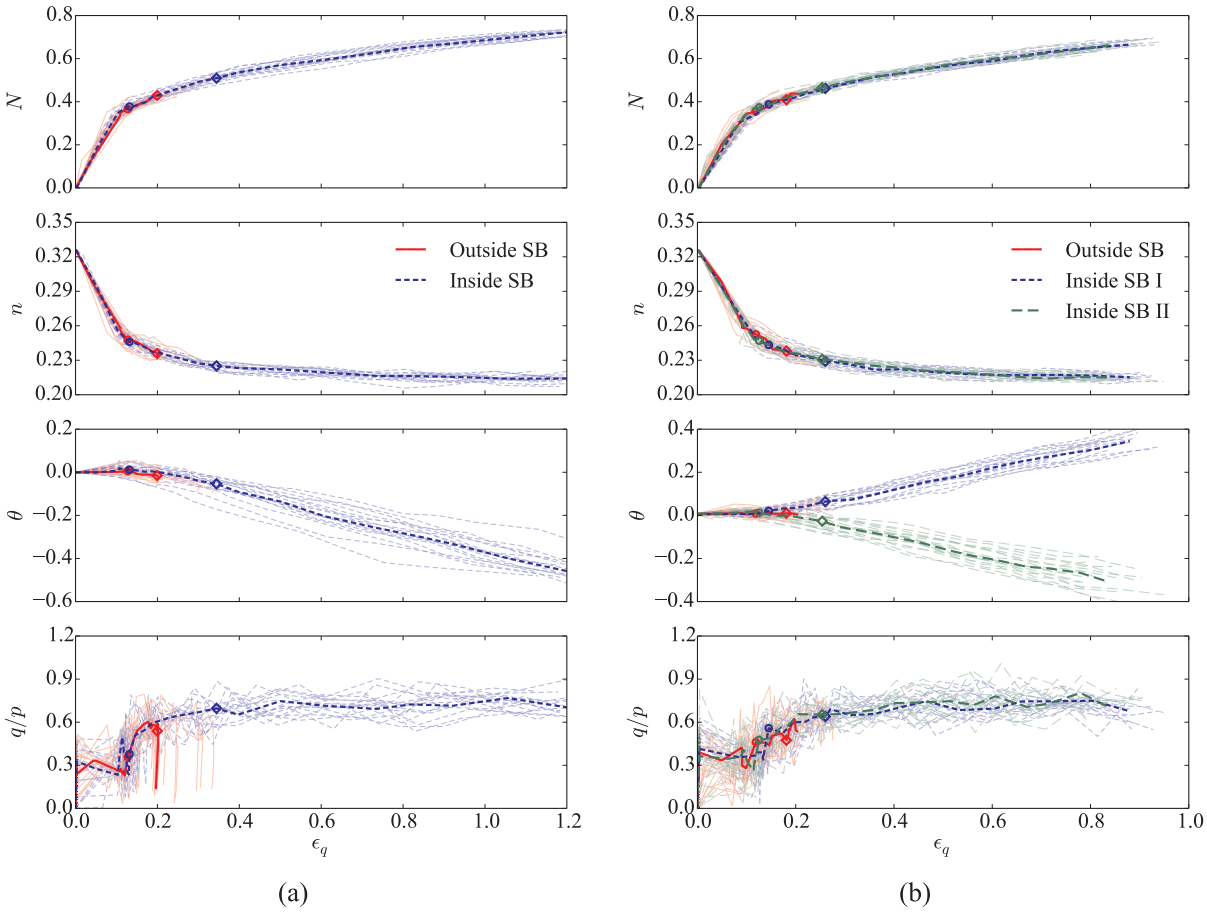

Fig. 9. The evolutions of local debonding number (N, normalized by initial bond number), porosity (n), average particle rotation (θ) and stress ratio (q/p) with deviatoric strain (ϵ_q) for (a) the smooth case and (b) the rough case at selected RVEs.

stage. N continues to increase at a decreasing rate and approaches to a steady state gradually.

Given the evolution of N with ϵ_q inside the SB, it is of particular interest to compare the steady state with the "critical state" observed for cohesionless sand. A DEM packing consisting of 40000 cohesionless particles is prepared for this purpose. All model parameters, including radii of the particles, interparticle contact model and model parameters, follow exactly the same as that for the high-porosity sandstone RVE as summarised in Table 1, except that no cohesion (bonding) is considered. Different initial porosities are reached by adjusting the interparticle friction during the isotropic compression stage. Similar approaches can be found in Guo and Zhao (2013). The generated specimens are subjected to quasi-static biaxial compression condition with the DEM solver and loaded to the critical state (final $\epsilon_1 = 50\%$). The homogenized responses of the dense, medium dense and loose specimens under $\sigma_0 = 40$ MPa with respect to increasing ϵ_q are shown in Fig. 10a. It is notable that all the specimens reach the same critical state with constant p, q and n. The void ratio ($e = n/(1-n)$) at the critical state in granular media depends on mean stress p following the general form [cf. (Zhao and Guo, 2013)]:

$$e_c = e_\Gamma - \lambda\left(\frac{p}{p_a}\right)^\xi \tag{4}$$

where e_c is the critical void ratio, e_Γ is the critical void ratio at $p = 0$, λ and ξ are material constants, and $p_a = 101$ kPa is the atmospheric pressure. A series of biaxial simulations under different σ_0 are conducted to obtain the critical void ratio under different p as illustrated in Fig. 10b. Our data fit Eq. (4) well with $e_\Gamma = 0.242$, $\lambda = 2.17 \times 10^{-8}$ and $\xi = 1.62$, presenting as the critical state line in Fig. 10b. Note that the critical state line is plotted up to a rather high mean stress given the large contact stiffness calibrated for sandstones. Possible grain crushing (ignored in the current study) may cause grading evolution and lead to an increase in λ, i.e. a smaller e_c at higher p (Ciantia et al., 2019).

The steady states in the three SBs observed in both smooth and rough cases are plotted as red diamonds in Fig. 10b. A discontinuous vertical axes is adopted to cover the large void ratio range. The steady void ratio in SBs (e_s^{SB}), under mean stress p at around 57.7 MPa, is around 0.277, as compared to a reference critical void ratio ($e_c^{Sand} = 0.241$) following Eq. (4). Notably, e_s^{SB} is even larger than the initial void ratio of the loose sample ($e_0 = 0.261$) under $\sigma_0 = 40$ MPa. The materials within the SBs would have approached a steady state equivalent to the critical state of the reference cohesionless sand, if all interparticle bonds were assumed to break at steady state. In this case, the steady void ratio inside the SBs is expected to further drop to be the same as (or at least close to) the critical state void ratio of the reference sand at the same p. The fact that $e_s^{SB} > e_c^{Sand}$ disproves this assumption and supports that not all interparticle bonds may have to break in the three SBs formed under sustained biaxial loading, i.e. N is indeed approaching a steady value smaller than 1.0 in Fig. 9. The particles bonded by the residual bonds may act as "nonspherical clumps", presenting some "shape" effects and leading to the larger e_s^{SB}. Possible reasons will be discussed based on microstructural analyses in the following section. Other complex loading conditions, e.g. cyclic loading, may be needed to break all the interparticle bonds.

4.3. Evolution of microstructure

Taking advantage of the capability of the multiscale approach for cross-scale analysis, we further examine the microstructural changes of

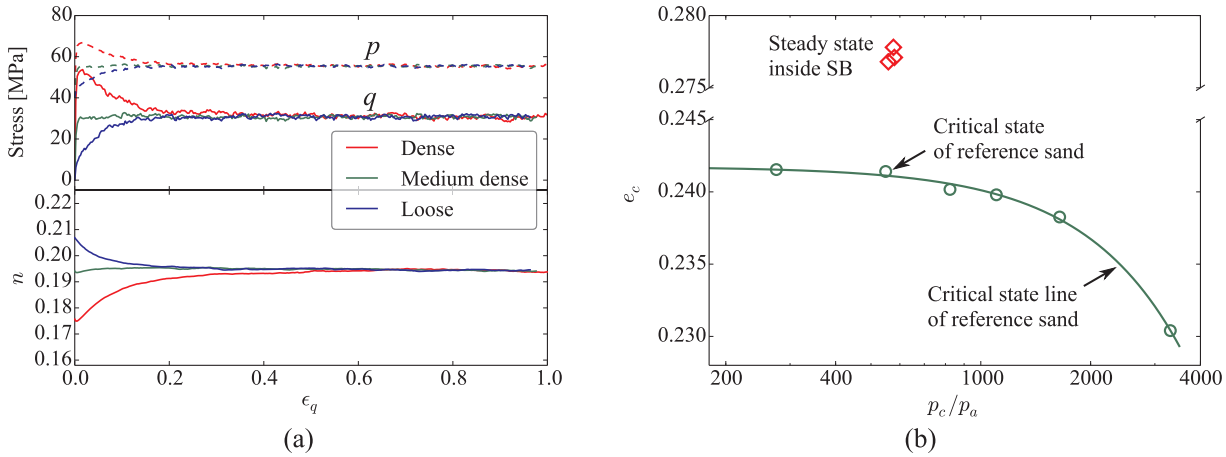

Fig. 10. Responses of reference sand subjected to biaxial compression towards critical state in DEM simulations. (a) Evolution of mean stress (p), deviatoric stress (q) and porosity (n) vs. deviatoric strain (ϵ_q) under confining pressure $\sigma_0 = 40$ MPa. (b) Critical state line of reference sand in the $e - p$ plane. The red diamonds mark the steady states reached inside SBs as presented in Fig. 9. (For interpretation of the references to color in this figure legend, the reader is referred to the web version of this article.)

selected RVEs during the transition from the CB stage to the SB stage and at the steady state attained. The force chain network has been popularly used in DEM studies to visualise the configurational changes of a granular packing, and will be adopted here for similar purposes. As a baseline reference, the force chain network of the initial RVE is presented in Fig. 1, which shows a largely isotropic distribution of contacts and macropores. The microscale responses of a typical RVE inside the shear band in the smooth case (see the white star in Fig. 4o) is illustrated in Fig. 11. Fig. 11a shows the RVE packing at the end of the CB stage which depicts by pure vertical compaction along the loading direction with no horizontal extension, shear or rigid rotation. Notably, the macropores in the initial RVE collapse and the intact cohesive contact network degrades to clusters and chains of various lengths. The distributions of the contact directions are shown in Fig. 11b where the blue sectors show for all the contacts and the red are for the cohesive ones. As shown, after the formation of CB, both contacts are found generally isotropic. Fig. 11c displays the RVE packing at the final state of shear band, featuring significant shear and rotation. The packing appears to be compressed with less appreciable macropores than the one in Fig. 11a. Moreover, the cohesive contact network degrades further to scattered clusters and shorter chains. Fig. 11d shows the distributions of the contact directions. while an appreciable preference along the vertical direction is observed for all contacts, a dominance along the horizontal direction is noted for the remnant cohesive contacts. The evolution of the directional distribution for cohesive contacts from the initial intact network to the final state is shown in Fig. 11f. It presents clearly a substantial reduction of cohesive contacts along all directions, and a gradual change of these contacts from a largely isotropic distribution at the initial state, to a rotation of around 30° at the end of the CB stage, and a final state with dominant horizontal contacts. The probability distributions of individual particle rotation (θ_p) are presented in Fig. 11e. Particle rotation indeed occurs even during the CB stage. Nevertheless, θ_p at the end of the CB stage is symmetrical with respect to 0 and more than half of the particles present a vanishing small rotation ($\theta_p \in [-0.42, 0.42]$). By contrast, θ_p at the final state is more spread presenting a flatter distribution with a deviation to the negative side, in agreement with the clockwise rigid rotation of the RVE as shown in Fig. 11c.

The material responses inside a single branch of the double SBs in the rough case are similar with those in the smooth case except the particle rotation direction in SB I is a positive. It is particularly interesting to look into the intersection of the double bands. The microscale responses of such an RVE (see the white star in Fig. 5o) is presented in Fig. 12. As expected, no major difference is observed at the end of the CB stage as compared to the selected one in the smooth case. However, the RVE packing at the final state as shown in Fig. 12c shows distinct features, i.e. with vertical compaction and horizontal extension. Less cohesive contacts, no apparent shear or rigid rotation are observed due to the counter effect of the symmetrical double bands, as compared to the single band in the smooth case. The distribution of the contact directions is similar with the one in the smooth case and the remnant cohesive contacts are even less. It is noteworthy that the rotation of individual particles (θ_p) may be significantly larger at the final state although the average particle rotation (θ) is around 0. See the distributions of θ_p in Fig. 12e.

The above microscale analyses reveal that the micromechanism during the re-hardening and the SB stage is distinct from that in the CB stage. During the CB stage, the micromechanism is dominated by interparticle debonding and macropore collapse, presenting a linear increase in N, linear decrease in n with loading and no apparent particle rotation. However, the SB stage is dominated by debonding and particle rotation with N, n and q gradually approaching steady states. The re-hardening stage reflects a transition of the micromechanism from pore collapse to particle rotation. The transition occurs around $n = 0.23$ and $N = 0.45$ in our presented example, when the reduced porosity prevents further pore collapse and more debonded particles facilitates the rotation of individual particles. Nevertheless, it is observed that some interparticle bonds persist at the steady state in SBs, even at the intersection of the double bands, with a preferential direction perpendicular to the loading direction. The presence of anisotropy helps explain the persistence of remnant interparticle bonds at the steady state which contributes to the difference between e_s^{SB} and e_c^{Sand}.

5. Conclusions

A coupled FEM/DEM multiscale approach based on bonded circular disks has been employed to investigate the evolution of localized deformation patterns in high-porosity sandstones under sustained biaxial loading. Two cases with smooth and rough boundary conditions have been considered for a specimen under biaxial compression, leading respectively two different formation of compaction band. The smooth case shows an initiation of compaction band from the middle of the specimen, while the rough case is from the two ends of the specimen. Further evolution of the initiated compaction bands and their gradual transitions to shear band through an intermediate re-hardening stage have been captured under sustained biaxial shear. Multiscale analyses have been carried out to explore the microstructural origins underscoring the pattern transition. Major findings over the different stages

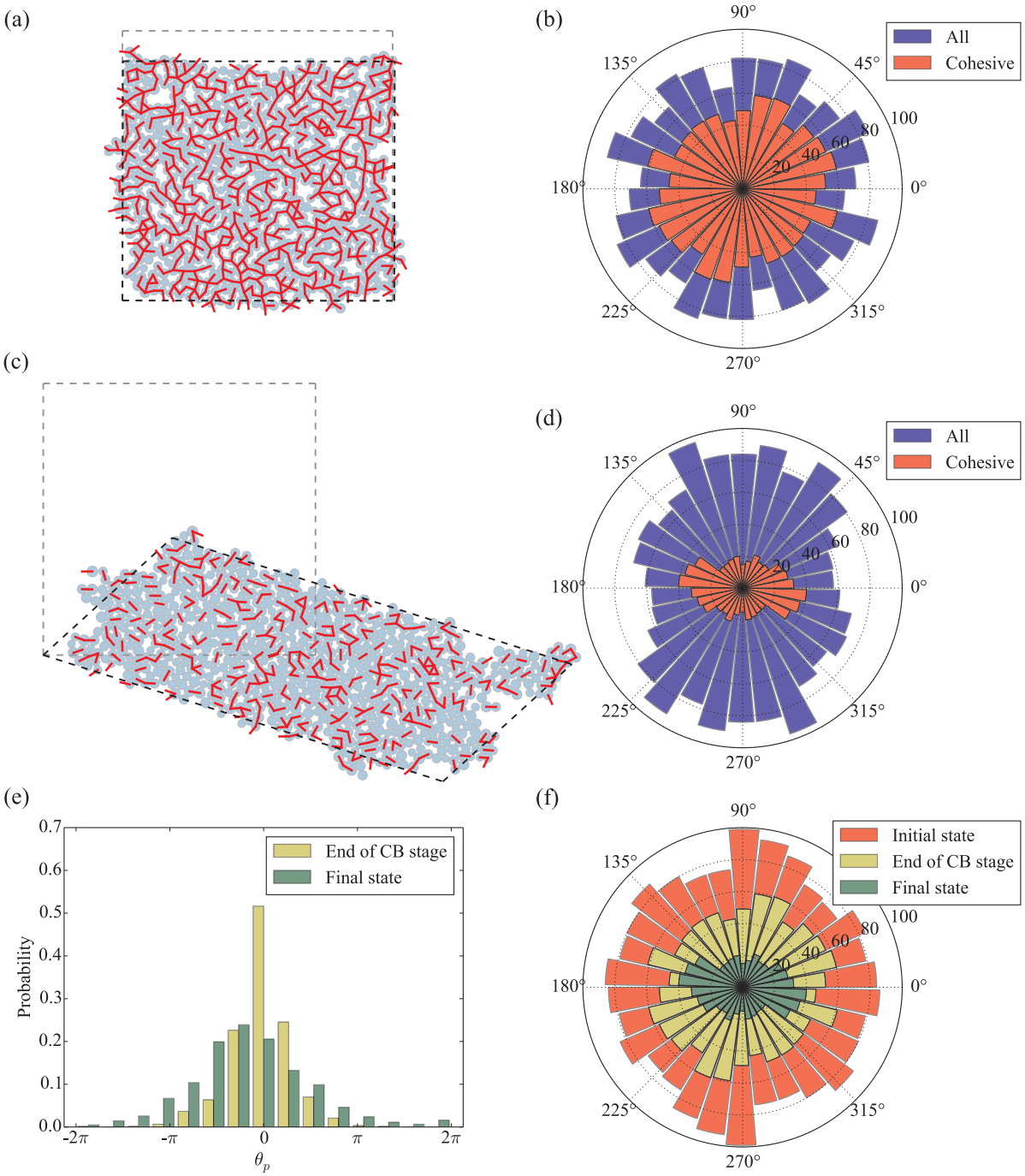

Fig. 11. Microscale responses of a typical RVE inside SB in the smooth case. RVE structure and the distribution of the contact directions (a–b) at the end of the CB stage and (c–d) at the final state. (e) Probability distributions of the individual particle rotation (θ_p). (f) Evolution of the direction distribution for cohesive contacts. In (a) and (c), the gray square marks the initial state and the red short lines indicate the cohesive contacts. (For interpretation of the references to color in this figure legend, the reader is referred to the web version of this article.)

from compaction band transiting to shear band are summarized below:

1. The propagation of compaction bands in both cases is characterized by steady propagation of compaction fronts that separates the compacted zone from the rest uncompacted zone in the specimen. The average pseudo velocity of the compaction front in the multiscale simulation agrees with analytical predictions by a simplified model based on mass conservation. The compaction fronts propagate and traverse the entire specimen to reach a roughly homogeneous state of lower porosity for the specimen. The duration of the compaction band stage in terms of axial strain level can be predicted by the initial porosity and the porosity of the compacted zone.
2. Further shear loading on the specimen leads to a re-hardening response of the entire specimen before the emergence of shear band localisation. The shear band(s) further develop and intensify to form final highly localised shear band(s). Mesoscale analyses reveal that the RVEs inside the shear bands approach a “steady state” of constant porosity and stress ratio with continuously increasing deviatoric strain. The steady void ratio is significantly higher than the critical state void ratio of the corresponding reference cohesionless sand, indicating the persistence of interparticle bonds at the steady

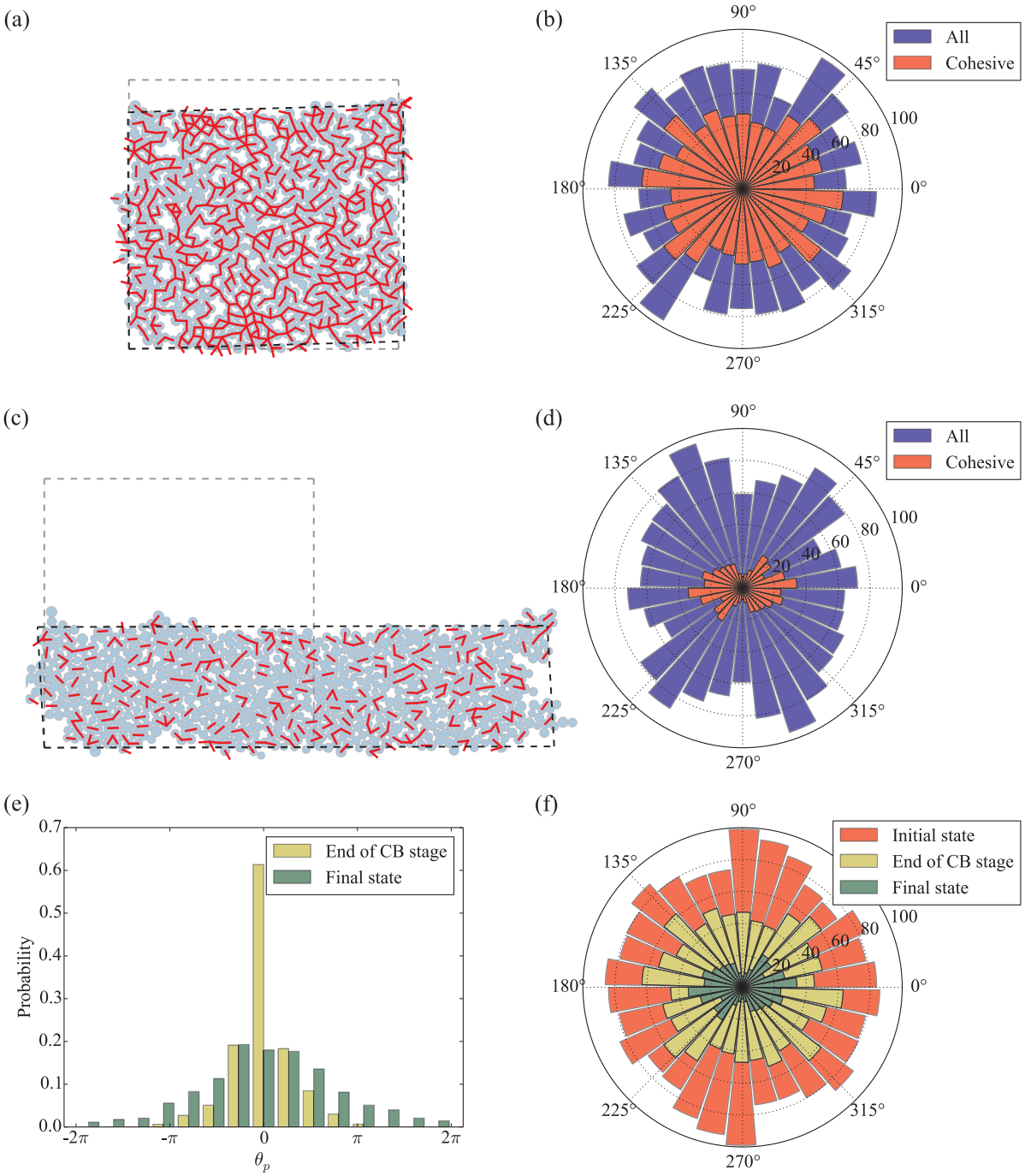

Fig. 12. Microscale responses of a RVE in the intersection of the double shear bands in the rough case. RVE structure and the distribution of the contact directions (a–b) at the end of the CB stage and (c–d) at the final state. (e) Probability distributions of the individual particle rotation (θ_p). (f) Evolution of the direction distribution for cohesive contacts. In (a) and (c), the gray square marks the initial state and the red short lines indicate the cohesive contacts. (For interpretation of the references to color in this figure legend, the reader is referred to the web version of this article.)

state in sandstone under sustained biaxial loading.

3. Microscale responses of the selected RVEs inside the shear band (s) help shed lights into the understanding of the transition from compaction band to shear band. The micromechanisms in compaction band stage is dominated by interparticle debonding and macropore collapse, whereas the shear band stage is dominated by debonding and particle rotation with debonding number, porosity and stress ratio approaching steady states. The transition occurs when the porosity reduction prevents further pore collapse while debonding facilitates the rotation of debonded particles. The remnant interparticle bonds in the shear bands, presenting a preferential direction perpendicular to the loading direction, are responsible for the higher steady void ratio than critical state.

Despite the successful reproduction of compaction band and its further transition to shear bands, the framework employed in this study does have its limitations. While we have adopted high-porosity RVE consisting of non-breakable circular particles to highlight the possibility of formation of compaction band due only to pore collapse and debonding in the absence of grain crushing. By no means would we exclude the importance of grain crushing in the initiation and formation of deformation bands, especially during the shear banding stage.

Indeed, our numerical simulations have predicted a rather brittle stress drop at the initiation of compaction band as compared to experimental observations (Wu et al., 2020b), which is duely attributable to the oversimplified RVE used. Predicting the macroscale responses based on faithful reproduction of the microscale properties and features of a granular medium, including the three dimensional particle shape and grain crushing, is a continuous pursuit for us. Possible directions to improve in this regard could be found in Guo and Zhao (2016b), Zhao and Zhao (2019a), Zhu and Zhao (2019b), Nie et al. (2020) and Shi et al. (2020).

CRediT authorship contribution statement

Huanran Wu: Methodology, Software, Data curation, Writing - original draft. **Jidong Zhao:** Conceptualization, Methodology, Supervision, Writing - review & editing. **Weijian Liang:** Visualization, Writing - review & editing.

Declaration of Competing Interest

The authors declare that they have no known competing financial interests or personal relationships that could have appeared to influence the work reported in this paper.

Acknowledgments

The study has been financially supported by the National Natural Science Foundation of China under project 51679207 and the Research Grants Council of Hong Kong through GRF project 16210017 and CRF CC6012-15G. HW has been financially supported by the National Natural Science Foundation of China under project 51922024. The software code used for modeling and generating the data in this study is based on the open-source parallel hierarchical multiscale modeling code FEM×DEM accessible via Yade (https://yade-dem.org/doc/FEMxDEM.html). All figures were generated by the open-source data analysis toolkit (Python with the NumPy/SciPy and matplotlib packages, Paraview and Inkscape).

References

Argilaga, A., Desrues, J., Pont, S.D., Combe, G., Caillerie, D., 2018. FEM×DEM multiscale modeling: Model performance enhancement from Newton strategy to element loop parallelization. International Journal for Numerical Methods in Engineering 114 (1), 47–65. https://doi.org/10.1002/nme.5732.

Aydin, A., 1978. Small faults formed as deformation bands in sandstone. Pure and Applied Geophysics PAGEOPH 116 (4–5), 913–930. https://doi.org/10.1007/BF00876546.

Aydin, A., Ahmadov, R., 2009. Bed-parallel compaction bands in aeolian sandstone: Their identification, characterization and implications. Tectonophysics 479 (3–4), 277–284. https://doi.org/10.1016/j.tecto.2009.08.033.

Barraclough, T.W., Blackford, J.R., Liebenstein, S., Sandfeld, S., Stratford, T.J., Weinländer, G., Zaiser, M., 2016. Propagating compaction bands in confined compression of snow. Nature Physics 13 (3), 272–275. https://doi.org/10.1038/nphys3966.

Baud, P., Klein, E., Wong, T.-F., 2004. Compaction localization in porous sandstones: Spatial evolution of damage and acoustic emission activity. Journal of Structural Geology 26 (4), 603–624. https://doi.org/10.1016/j.jsg.2003.09.002.

Baud, P., Meredith, P., Townend, E., 2012. Permeability evolution during triaxial compaction of an anisotropic porous sandstone. Journal of Geophysical Research 117, B05203. https://doi.org/10.1029/2012JB009176.

Baud, P., Reuschlé, T., Ji, Y., Cheung, C.S.N., Wong, T.-F., 2015. Mechanical compaction and strain localization in Bleurswiller sandstone. Journal of Geophysical Research: Solid Earth 120 (9), 6501–6522. https://doi.org/10.1002/2015JB012192.

Buscarnera, G., Laverack, R.T., 2014. Path dependence of the potential for compaction banding: Theoretical predictions based on a plasticity model for porous rocks. Journal of Geophysical Research: Solid Earth 119 (3), 1882–1903. https://doi.org/10.1002/2013JB010562.

Cheung, C.S.N., Baud, P., Wong, T.-F., 2012. Effect of grain size distribution on the development of compaction localization in porous sandstone. Geophysical Research Letters 39 (21), 6–10. https://doi.org/10.1029/2012GL053739.

Ciantia, M.O., Arroyo, M., O'Sullivan, C., Gens, A., Liu, T., 2019. Grading evolution and critical state in a discrete numerical model of Fontainebleau sand. Géotechnique 69 (1), 1–15. https://doi.org/10.1680/jgeot.17.P.023.

Das, A., Tengattini, A., Nguyen, G.D., Viggiani, G., Hall, S.A., Einav, I., 2014. A thermomechanical constitutive model for cemented granular materials with quantifiable internal variables. Part II – Validation and localization analysis. Journal of the Mechanics and Physics of Solids 70 (1), 382–405. https://doi.org/10.1016/j.jmps.2014.05.022.

Desrues, J., Argilaga, A., Dal Pont, S., Combe, G., Caillerie, D., kein Nguyen, T., 2017. Restoring mesh independency in FEM-DEM multi-scale modelling of strain localization using second gradient regularization. In: Papamichos, E., Papanastasiou, P., Pasternak, E., Dyskin, A. (Eds.), Bifurcation and Degradation of Geomaterials with Engineering Applications. Springer Series in Geomechanics and Geoengineering Springer International Publishing, pp. 453–457 doi:978-3-319-56397-8_57.

Desrues, J., Argilaga, A., Caillerie, D., Combe, G., Nguyen, T.K., Richefeu, V., Pont, S.D., 2019. From discrete to continuum modelling of boundary value problems in geomechanics: An integrated FEM-DEM approach. International Journal for Numerical and Analytical Methods in Geomechanics 43 (5), 919–955. https://doi.org/10.1002/nag.2914.

Eichhubl, P., Hooker, J.N., Laubach, S.E., 2010. Pure and shear-enhanced compaction bands in Aztec Sandstone. Journal of Structural Geology 32 (12), 1873–1886. https://doi.org/10.1016/j.jsg.2010.02.004.

Fortin, J., Stanchits, S., Dresen, G., Guéguen, Y., 2006. Acoustic emission and velocities associated with the formation of compaction bands in sandstone. Journal of Geophysical Research 111, B10203. https://doi.org/10.1029/2005JB003854.

Fossen, H., 2010. Structural Geology. Cambridge University Press, New York.

Fossen, H., Bale, A., 2007. Deformation bands and their influence on fluid flow. AAPG Bulletin 91 (12), 1685–1700. https://doi.org/10.1306/07300706146.

Gao, Z., Zhao, J., 2013. Strain localization and fabric evolution in sand. International Journal of Solids and Structures 50 (22–23), 3634–3648. https://doi.org/10.1016/j.ijsolstr.2013.07.005.

Guillard, F., Golshan, P., Shen, L., Valdes, J.R., Einav, I., 2015. Dynamic patterns of compaction in brittle porous media. Nature Physics 11 (10), 835–838. https://doi.org/10.1038/nphys3424.

Guo, N., Zhao, J., 2013. The signature of shear-induced anisotropy in granular media. Computers and Geotechnics 47, 1–15. https://doi.org/10.1016/j.compgeo.2012.07.002.

Guo, N., Zhao, J., 2014. A coupled FEM/DEM approach for hierarchical multiscale modelling of granular media. International Journal for Numerical Methods in Engineering 99 (11), 789–818. https://doi.org/10.1002/nme.4702.

Guo, N., Zhao, J., 2016a. Multiscale insights into classical geomechanics problems. International Journal for Numerical and Analytical Methods in Geomechanics 40 (3), 367–390. https://doi.org/10.1002/nag.2406.

Guo, N., Zhao, J., 2016b. 3D multiscale modeling of strain localization in granular media. Computers and Geotechnics 80, 360–372. https://doi.org/10.1016/j.compgeo.2016.01.020.

Guo, N., Zhao, J., 2016c. Parallel hierarchical multiscale modelling of hydro-mechanical problems for saturated granular soils. Computer Methods in Applied Mechanics and Engineering 305 (9), 768–785. https://doi.org/10.1016/j.cma.2016.03.004.

Guo, N., Zhao, J., Sun, W., 2016. Multiscale analysis of shear failure of thick-walled hollow cylinder in dry sand. Géotechnique Letters 6 (1), 1–18. https://doi.org/10.1680/jgele.15.00149.

Haimson, B.C., 2003. Borehole Breakouts in Berea Sandstone Reveal a New Fracture Mechanism. Pure and Applied Geophysics 160, 813–831. https://doi.org/10.1007/PL00012567.

Haimson, B.C., 2007. Micromechanisms of borehole instability leading to breakouts in rocks. International Journal of Rock Mechanics and Mining Sciences 44 (2), 157–173. https://doi.org/10.1016/j.ijrmms.2006.06.002.

Haimson, B.C., Lee, H., 2004. Borehole breakouts and compaction bands in two high-porosity sandstones. International Journal of Rock Mechanics and Mining Sciences 41 (2), 287–301. https://doi.org/10.1016/j.ijrmms.2003.09.001.

Holcomb, D., Rudnicki, J.W., Issen, K.A., Sternlof, K., 2007. Compaction localization in the Earth and the laboratory: State of the research and research directions. Acta Geotechnica 2 (1), 1–15. https://doi.org/10.1007/s11440-007-0027-y.

Issen, K.A., Challa, V., 2008. Influence of the intermediate principal stress on the strain localization mode in porous sandstone. Journal of Geophysical Research: Solid Earth 113 (B2). https://doi.org/10.1029/2005JB004008.

Issen, K.A., Rudnicki, J.W., 2000. Conditions for compaction bands in porous rock. Journal of Geophysical Research 105 (B9), 21529–21536. https://doi.org/10.1029/2000JB900185.

Jiang, M.J., Yan, H.B., Zhu, H.H., Utili, S., 2011. Modeling shear behavior and strain localization in cemented sands by two-dimensional distinct element method analyses. Computers and Geotechnics 38 (1), 14–29. https://doi.org/10.1016/j.compgeo.2010.09.001.

Katsman, R., Aharonov, E., Scher, H., 2006. Localized compaction in rocks: Eshelby's inclusion and the Spring Network Model. Geophysical Research Letters 33 (10), 1–5. https://doi.org/10.1029/2005GL025628.

Liu, C., Pollard, D.D., Gu, K., Shi, B., 2015. Mechanism of formation of wiggly compaction bands in porous sandstone: 2. Numerical simulation using discrete element method. Journal of Geophysical Research: Solid Earth 120 (12), 8153–8168. https://doi.org/10.1002/2015JB012374.

Liu, Y., Sun, W., Yuan, Z., Fish, J., 2016. A nonlocal multiscale discrete-continuum model for predicting mechanical behavior of granular materials. International Journal for Numerical Methods in Engineering 106 (2), 129–160. https://doi.org/10.1002/nme.5139.

Mollema, P.N., Antonellini, M.A., 1996. Compaction bands: A structural analog for anti-mode I cracks in aeolian sandstone. Tectonophysics 267 (1–4), 209–228. https://doi.org/10.1016/S0040-1951(96)00098-4.

Nie, J.-Y., Li, D.-Q., Cao, Z.-J., Zhou, B., Zhang, A.-J., 2020. Probabilistic characterization and simulation of realistic particle shape based on sphere harmonic representation

and Nataf transformation. Powder Technology 360, 209–220. https://doi.org/10.1016/j.powtec.2019.10.007.
Olsson, W.A., 1999. Theoretical and experimental investigation of compaction bands in porous rock. Journal of Geophysical Research 104 (B4), 7219–7228. https://doi.org/10.1029/1998JB900120.
Olsson, W.A., 2001. Quasistatic propagation of compaction fronts in porous rock. Mechanics of Materials 33 (11), 659–668. https://doi.org/10.1016/S0167-6636(01)00078-3.
Olsson, W.A., Holcomb, D.J., 2000. Compaction localization in porous rock. Geophysical Research Letters 27 (21), 3537–3540. https://doi.org/10.1029/2000GL011723.
Papazoglou, A., 2018. An experimental study of localized compaction in high porosity rocks: The example of Tuffeau de Maastricht, PhD thesis, Université Grenoble Alpes, Grenoble.
Schaa, R., Gross, L., du Plessis, J., 2016. PDE-based geophysical modelling using finite elements: Examples from 3D resistivity and 2D magnetotellurics. Journal of Geophysics and Engineering 13 (2), S59. https://doi.org/10.1088/1742-2132/13/2/S59.
Schofield, A., Wroth, P., 1968. Critical State Soil Mechanics. McGraw-Hill, London, UK.
Schultz, R.A., Okubo, C.H., Fossen, H., 2010. Porosity and grain size controls on compaction band formation in Jurassic Navajo Sandstone. Geophysical Research Letters 37 (22), 1–5. https://doi.org/10.1029/2010GL044909.
Shahin, G., Desrues, J., Pont, S.D., Combe, G., Argilaga, A., 2016. A study of the influence of REV variability in double-scale FEM ×DEM analysis. International Journal for Numerical Methods in Engineering 107 (10), 882–900. https://doi.org/10.1002/nme.5202.
Shahin, G., Papazoglou, A., Marinelli, F., Buscarnera, G., 2019. Simulation of localized compaction in Tuffeau de Maastricht based on evidence from X-ray tomography. International Journal of Rock Mechanics and Mining Sciences 121, 104039 https://doi.org/10.1016/j.ijrmms.2019.05.005.
Shi, X.S., Nie, J., Zhao, J., Gao, Y., 2020. A homogenization equation for the small strain stiffness of gap-graded granular materials. Computers and Geotechnics 121, 103440 https://doi.org/10.1016/j.compgeo.2020.103440.
Smilauer, V., Catalano, E., Chareyre, B., Dorofeenko, S., Duriez, J., Dyck, N., Elias, J.,Er, B., Eulitz, A., Gladky, A., Jakob, C., Kneib, F., Kozicki, J., Marzougui, D., Maurin, R., Modenese, C., Scholtes, L., Sibille, L., Stransky, J., Sweijen, T., Thoeni, K., Yuan, C., 2015. Yade Documentation. second ed. The Yade Project. doi:10.5281/zenodo.34073.
Tembe, S., Baud, P., Wong, T.-F., 2008. Stress conditions for the propagation of discrete compaction bands in porous sandstone. Journal of Geophysical Research 113, B09409. https://doi.org/10.1029/2007JB005439.
Townend, E., Thompson, B.D., Benson, P.M., Meredith, P.G., Baud, P., Young, R.P., 2008. Imaging compaction band propagation in Diemelstadt sandstone using acoustic emission locations. Geophysical Research Letters 35 (15), 1–5. https://doi.org/10.1029/2008GL034723.
Vajdova, V., Baud, P., Wong, T.-F., 2004. Permeability evolution during localized deformation in Bentheim sandstone. Journal of Geophysical Research 109, B10406. https://doi.org/10.1029/2003JB002942.
Valdes, J.R., Fernandes, F.L., Einav, I., 2012. Periodic propagation of localized compaction in a brittle granular material. Granular Matter 14 (1), 71–76. https://doi.org/10.1007/s10035-011-0302-3.
Wang, Y.-H., Leung, S.-C., 2008. A particulate-scale investigation of cemented sand behavior. Canadian Geotechnical Journal 45 (1), 29–44. https://doi.org/10.1139/T07-070.
Wang, K., Sun, W., 2016. A semi-implicit discrete-continuum coupling method for porous media based on the effective stress principle at finite strain. Computer Methods in Applied Mechanics and Engineering 304, 546–583. https://doi.org/10.1016/j.cma.2016.02.020.
Wong, T.-F., Szeto, H., Zhang, J., 1992. Effect of loading path and porosity on the failure mode of porous rocks. Applied Mechanics Reviews 45 (8), 281–293. https://doi.org/10.1115/1.3119759.
Wu, H., Guo, N., Zhao, J., 2017. Borehole Instabilities in Granular Rocks Revisited: A Multiscale Perspective. In: Papamichos, E., Papanastasiou, P., Pasternak, E., Dyskin, A. (Eds.), Bifurcation and Degradation of Geomaterials with Engineering Applications. Springer Series in Geomechanics and Geoengineering, Springer, Cham, pp. 433–439.
Wu, H., Guo, N., Zhao, J., 2018a. Multiscale modeling and analysis of compaction bands in high-porosity sandstones. Acta Geotechnica 13 (3), 575–599. https://doi.org/10.1007/s11440-017-0560-2.
Wu, H., Zhao, J., Guo, N., 2018b. Multiscale Insights Into Borehole Instabilities in High-Porosity Sandstones. Journal of Geophysical Research: Solid Earth 123 (5), 3450–3473. https://doi.org/10.1029/2017JB015366.
Wu, H., Zhao, J., Guo, N., 2019. Multiscale modeling of compaction bands in saturated high-porosity sandstones. Engineering Geology 261, 105282 https://doi.org/10.1016/j.enggeo.2019.105282.
Wu, H., Zhao, J., Liang, W., 2020a. The signature of deformation bands in porous sandstones. Rock Mechanics and Rock Engineering. https://doi.org/10.1007/s00603-020-02100-8.
Wu, H., Papazoglou, A., Viggiani, G., Dano, C., Zhao, J., 2020b. Compaction bands in Tuffeau de Maastricht: Insights from X-ray tomography and multiscale modeling. Acta Geotechnica 15 (1), 39–55. https://doi.org/10.1007/s11440-019-00904-9.
Zhao, J., Guo, N., 2013. Unique critical state characteristics in granular media considering fabric anisotropy. Géotechnique 8 (8), 695–704. https://doi.org/10.1680/geot.12.P.040.
Zhao, J., Guo, N., 2015. The interplay between anisotropy and strain localisation in granular soils: A multiscale insight. Géotechnique 65 (8), 642–656. https://doi.org/10.1680/geot.14.P.184.
Zhao, S., Zhao, J., 2019a. A poly-superellipsoid-based approach on particle morphology for DEM modeling of granular media. International Journal for Numerical and Analytical Methods in Geomechanics 43 (13), 2147–2169. https://doi.org/10.1002/nag.2951.
Zhu, F., Zhao, J., 2019b. Modeling continuous grain crushing in granular media: A hybrid peridynamics and physics engine approach. Computer Methods in Applied Mechanics and Engineering 348, 334–355. https://doi.org/10.1016/j.cma.2019.01.017.